

Quasiparticle Interference and Symmetry of Superconducting Order Parameter in Strongly Electron-Doped Iron-based Superconductors

Jakob Böker¹, Pavel A. Volkov^{2,1}, P. J. Hirschfeld³, and Ilya Eremin¹

1-Institut für Theoretische Physik III, Ruhr-Universität Bochum, D-44801 Bochum, Germany

2-Department of Physics and Astronomy, Center for Materials Theory,

Rutgers University, Piscataway, New Jersey 08854, USA and

3-Department of Physics, University of Florida, Gainesville, Florida 32611, USA

(Dated: July 30, 2019)

Motivated by recent experimental reports of significant spin-orbit coupling (SOC) and a sign-changing order-parameter in the $\text{Li}_{1-x}\text{Fe}_x(\text{OHFe})_{1-y}\text{Zn}_y\text{Se}$ superconductor with only electron pockets present, we study the possible Cooper-pairing symmetries and their quasiparticle interference (QPI) signatures. We find that each of the resulting states - s -wave, d -wave and helical p -wave - can have a fully gapped density of states (DOS) consistent with angle-resolved photoemission spectroscopy (ARPES) experiments and, due to spin-orbit coupling, are a mixture of spin singlet and triplet components leading to intra- and inter-band features in the QPI signal. Analyzing predicted QPI patterns we find that only the spin-triplet dominated even parity A_{1g} (s -wave) and B_{2g} (d -wave) pairing states are consistent with the experimental data. Additionally, we show that these states can indeed be realized in a microscopic model with atomic-like interactions and study their possible signatures in spin-resolved STM experiments.

I. INTRODUCTION

In iron-based superconductors, it has been widely believed that superconductivity is driven by repulsive interactions, enhanced by the presence of the spin fluctuations associated with the parent antiferromagnetic state. In this scenario, these fluctuations drive a sign reversal (s_{\pm} state)¹⁻⁵ between order parameters (OP) on the electron and hole Fermi surface pockets at the M - and Γ -point, respectively. The discovery of superconductivity in intercalated or monolayer FeSe at a critical temperature of the order above 40K revived interest in Fe-based superconductivity, but raised further questions on the origin of superconductivity in these compounds⁶⁻¹⁰, because, unlike bulk FeSe, ARPES experiments show that many of these FeSe-derived systems appear to be missing the hole pockets at the Γ -point required in the the conventional scenario.

Initial model calculations based on the multiorbital spin-fluctuation framework for systems manifesting only electron pockets at the M -point predicted d -wave symmetry state in this case^{11,12}, driven by the spin fluctuations connecting the electron pockets that remain when the hole pockets are removed. In the proper 2-Fe unit cell, such a state must have gap nodes on the Fermi surface¹³. This is because the electron pockets located near $(\pi, 0)$ or $(0, \pi)$ points of the Brillouin Zone (BZ) in the 1-Fe unit cell fold onto (π, π) point of the folded BZ as the crystallographic symmetry lowers due to the Se positions. This may lead to hybridization between the electron pockets¹⁴, which then forces the $d_{x^2-y^2}$ -state to acquire gap nodes, although in principle the nodal area may be very small, proportional to the hybridization (“quasimodes”). On the other hand, ARPES experiments in most of the electron-intercalated materials indicated a nodeless superconducting (sc) state^{15,16}. Several proposals for the gap structure have been put forward, including a conventional s^{++} -wave scenario based on the electron-phonon interaction and orbital fluctuations¹⁷, as well as the “bonding-antibonding” scenario^{13,18} in which the order parameter on the inner electron pocket (mostly d_{xz}/d_{yz} character) has one sign, and on the outer electron pocket (mostly d_{xy} character) the other¹⁴. Furthermore, it has been argued that the hybridization of the electron pockets is mainly due to SOC¹⁹⁻²¹, which within a 3D spin fluctuation framework may stabilize the bonding-antibonding s_{\pm} state against d -wave¹⁹ and mixes a spin-triplet component into the even parity s^{+-} -wave state^{20,21}. Overall, one can see that the sign structure of the superconducting order parameter is intimately related to the pairing mechanism. Therefore, experiments allowing to determine it could be of great potential importance.

One rapidly developing technique to determine the phase structure of the order parameter makes use of QPI as measured by Fourier transform scanning tunneling microscopy (FT-STM). This probe measures the wavelengths of Friedel oscillations caused by impurities present in a metallic or superconducting system, which in turn contains information on the electronic structure of the pure system. A subset of scattering wave vectors \mathbf{q} corresponding to peaks in the FT-STM can be enhanced or not according to the type of disorder and the phase structure of the superconducting gap^{22,23}. Recently it was proposed by Hirschfeld, Altenfeld, Eremin and Mazin (HAEM)²⁴ that the sign structure of the order parameter in a multiband system can be extracted from the Fourier transform of the local density of states QPI pattern near an impurity in the superconducting state. The antisymmetrized QPI intensity integrated over the wavevectors corresponding to scattering between two bands was shown to have a dependence on frequency very different for sign-changing and sign preserving scenarios leading to a strong, single-sign enhancement of the integrated response in the former case. This qualitative result was also confirmed by extensive numerical simulations with finite disorder²⁵. Recently, a complementary phase sensitive technique to detect sign-changing gaps in the presence of strong impurity bound states was proposed²⁶.

Using QPI analysis, the authors of Ref. 27 were able to identify a sign changing order parameter in FeSe. Most importantly for our purposes, similar conclusions were recently drawn for the strongly electron doped iron-based superconductor lithium hydroxide intercalated FeSe²⁸. In other words, the order parameter in $\text{Li}_{1-x}\text{Fe}_x(\text{OHFe})_{1-y}\text{Zn}_y\text{Se}$, alternates sign, either between the Fermi surface sheets, or within individual sheets. However, distinguishing between these alternatives was beyond the resolution of the experiment. In any case, the situation is somewhat more complicated than anticipated in Ref. 28, since the effect of spin-orbit interaction on pairing needs to be taken into account as well. Moreover, recent observation of Majorana zero modes in $(\text{Li}_{0.84}\text{Fe}_{0.16})\text{OHFeSe}$ ²⁹ suggests possible broader implications of the spin-orbit coupling for the Cooper-pairing in electron doped intercalated iron-based superconductors. Note that in contrast to Ref. 28, no Zn substitution was used in Ref. 29. The amount of Zn, however, is relatively small (less than 2 percent). This amount does not affect the superconducting transition temperature or the electronic structure in a significant way and is done only for the purpose of enhancing the QPI signal in the scanning tunneling microscopy.

In this manuscript we study the possible Cooper-pairing symmetries and their QPI signatures for strongly electron-doped Fe-based superconductors using the effective three-orbital model of Refs. 20 and 21 with spin-orbit coupling and proper consideration of all lattice symmetries of the FeSe space group. We find that each of the resulting states - A_{1g} -wave, B_{2g} -wave and helical E_u -wave - can have a fully gapped DOS consistent with ARPES experiments and, due to spin-orbit coupling, are a mixture of spin singlet and triplet components leading to intra- and inter-band features in the QPI signal. Analyzing predicted QPI patterns we find that A_{1g} -wave pairing state, with the two dominant

peaks in the DOS roughly corresponding to the gap energies on each pocket, and B_{2g} -wave pairing state both with a significant even parity spin triplet component are consistent with the experimental data. Moreover, we show that pairing states with dominant spin triplet component can be identified using spin-resolved STM.

II. MODEL

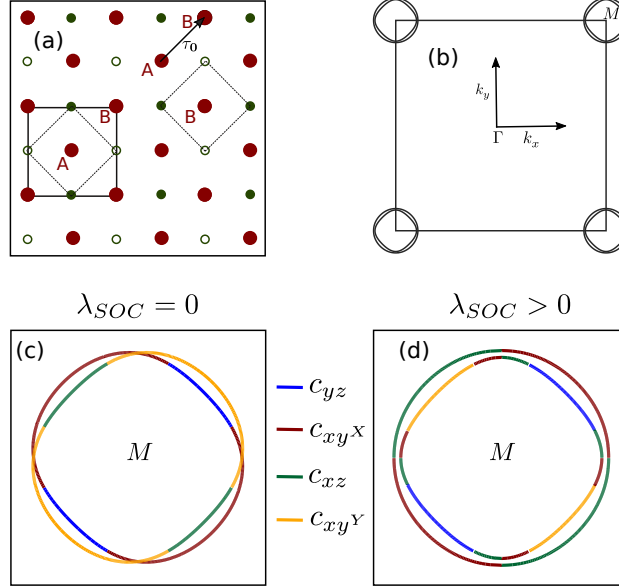


FIG. 1. (a) Single layer of the iron based superconductors lattice structure. Red and green dots are iron and pnictogen or Se atoms, respectively. One pnictogen sublattice is puckered above the iron layer (filled green dots) one is puckered below (empty green dots) which divides the iron atoms into sublattices A and B. One-iron unit cells for sublattices A and B are denoted by dashed squares. The two-iron unit cell, taking the puckering into account, is shown by the solid square. The vector τ_0 connects sublattices A and B. (b) Fermi surface of low-energy model consistent with Ref.10. (c) Pockets at M point without SOC corresponding to is X- and Y-pocket folded upon each other. (d) Pockets at M point with SOC $\lambda_{\text{SOC}} = 5$ meV. Inner and outer pocket in the presence of SOC, leading to lifted degeneracy at zone diagonals. The color scheme in (c),(d) follows majority orbital content.

We wish to describe the low energy states near the M-points of the Brillouin zone using the orbitally projected band model of Ref. 20 and 21 for the two-iron unit cell. Near the Fermi level, only the xz , yz and xy orbitals contribute significantly; hence, the full 10-orbital tight binding model is projected onto the subspace of these three orbitals. The effective low energy Hamiltonian near the M-point that takes into account all the lattice symmetries of the FeSe space group as well as time reversal symmetry is defined as

$$H = \sum_{\sigma, \sigma' = \uparrow, \downarrow} \sum_{\mathbf{k}} \Psi_{M, \sigma}^\dagger(\mathbf{k}) \begin{pmatrix} h_X'^{\sigma, \sigma'}(\mathbf{k}) & \Lambda_{\text{SOC}}^{\sigma, \sigma'} \\ \Lambda_{\text{SOC}}^{\dagger \sigma, \sigma'} & h_Y'^{\sigma, \sigma'}(\mathbf{k}) \end{pmatrix} \Psi_{M, \sigma'}(\mathbf{k}), \quad (1)$$

where the four component spinor $\Psi_{M, \sigma}^\dagger(\mathbf{k}) = (\Psi_{X, \sigma}^\dagger(\mathbf{k}), \Psi_{Y, \sigma}^\dagger(\mathbf{k}))$ describes the states at the M-point for each spin projection σ . The doublets $\Psi_{X, \sigma}(\mathbf{k})$ and $\Psi_{Y, \sigma}(\mathbf{k})$ are defined as

$$\Psi_{X, \sigma}(\mathbf{k}) = \begin{pmatrix} c_{yz, \sigma}(\mathbf{k}) \\ c_{xy^X, \sigma}(\mathbf{k}) \end{pmatrix}, \quad \Psi_{Y, \sigma}(\mathbf{k}) = \begin{pmatrix} c_{xz, \sigma}(\mathbf{k}) \\ c_{xy^Y, \sigma}(\mathbf{k}) \end{pmatrix} \quad (2)$$

Moreover, we have

$$\begin{aligned}
h_X^{\sigma\sigma'}(\mathbf{k}) &= h_X(\mathbf{k})\delta_{\sigma,\sigma'} + \left(\lambda_z(k_x - k_y) \right. \\
&\quad \left. + p_{z_1}(k_x^3 - k_y^3) + p_{z_2}k_xk_y(-k_x + k_y) \right) \sigma_{\sigma,\sigma'}^z \tau_1 \\
h_Y^{\sigma\sigma'}(\mathbf{k}) &= h_Y(\mathbf{k})\delta_{\sigma,\sigma'} + \left(\lambda_z(k_x + k_y) \right. \\
&\quad \left. + p_{z_1}(k_x^3 + k_y^3) + p_{z_2}k_xk_y(k_x + k_y) \right) \sigma_{\sigma,\sigma'}^z \tau_1
\end{aligned} \tag{3}$$

and

$$h_X(\mathbf{k}) = \begin{pmatrix} \epsilon_1 + \frac{\mathbf{k}^2}{2m_1} + \alpha_1 k_x k_y & -iv(k_x + k_y) \\ iv(k_x + k_y) & \epsilon_3 + \frac{\mathbf{k}^2}{2m_3} + \alpha_3 k_x k_y \end{pmatrix}, \tag{4}$$

$$h_Y(\mathbf{k}) = \begin{pmatrix} \epsilon_1 + \frac{\mathbf{k}^2}{2m_1} - \alpha_1 k_x k_y & -iv(-k_x + k_y) \\ iv(-k_x + k_y) & \epsilon_3 + \frac{\mathbf{k}^2}{2m_3} - \alpha_3 k_x k_y \end{pmatrix} \tag{5}$$

where the Pauli matrices $\{\sigma^x, \sigma^y, \sigma^z\}$ and $\{\tau_1, \tau_2, \tau_3\}$ act on spin and orbital space, respectively. The λ_z , p_{z_1} and p_{z_2} terms in eq.(3) describe the k-dependent intra-band SOC which does not couple the two Fermi pockets but lifts the out-of plane spin degeneracy. The inter-band SOC term which hybridizes X- and Y-pocket is given by

$$\Lambda_{\text{SOC}}^{\sigma,\sigma'} = i\lambda_{\text{SOC}} \left(\frac{\tau_1 + i\tau_2}{2} \otimes \sigma_{\sigma,\sigma'}^x + \frac{\tau_1 - i\tau_2}{2} \otimes \sigma_{\sigma,\sigma'}^y \right). \tag{6}$$

In order to describe intercalated FeSe we use the Luttinger invariants, Tab.(I), which were evaluated in Ref.21 based on the available ARPES data.

α_1	782.512 meV \AA^2
α_3	-1400 meV \AA^2
$\frac{1}{2m_1}$	-492.01 meV \AA^2
$\frac{1}{2m_3}$	1494.14 meV \AA^2
v	224.406 meV \AA
λ_z	26 meV
$p_{z_1} = p_{z_3}$	0

TABLE I. Fitting parameters relevant for intercalated FeSe taken from Ref.21.

The value of the intraband spin-orbit coupling, λ_z is in agreement with those found in ab-initio calculations and ARPES experiments^{30,31}. Furthermore, the value of the interband spin-orbit coupling, λ_{SOC} between the electron pockets separated by the large momentum yielding their hybridization and splitting on the Fermi surface is found to be smaller and is taken to be ~ 5 meV³¹.

Diagonalizing Eq.(1) yields four bands: two regular ones that form the inner and outer electron pocket, see Fig.1(b), and two incipient bands that do not cross the Fermi level. The effect of inter-band SOC on the band structure is visualized in Fig.1(c) and Fig.1(d).

III. MEAN FIELD PHASE DIAGRAM

Although phenomenologically the classification of superconducting orders for two electron pockets was considered previously^{20,21} we analyze here its microscopic formulation via mean-field treatment of the atomic on-site interactions

given by the Hubbard and Hund's couplings U , U' , J and J' which enter the Hubbard-Kanamori Hamiltonian as

$$\begin{aligned}
H_{\text{int}}(\mathbf{r}) = & \sum_{\alpha} \sum_{\mu} U_{\mu\mu} d_{\mu,\uparrow}^{\alpha\dagger}(\mathbf{r}) d_{\mu,\downarrow}^{\alpha\dagger}(\mathbf{r}) d_{\mu,\downarrow}^{\alpha}(\mathbf{r}) d_{\mu,\uparrow}^{\alpha}(\mathbf{r}) \\
& + \sum_{\mu \neq \nu} J'_{\mu\nu} d_{\mu,\uparrow}^{\alpha\dagger}(\mathbf{r}) d_{\mu,\downarrow}^{\alpha\dagger}(\mathbf{r}) d_{\nu,\downarrow}^{\alpha}(\mathbf{r}) d_{\nu,\uparrow}^{\alpha}(\mathbf{r}) \\
& + \sum_{\mu < \nu} \sum_{\sigma, \sigma'} \frac{J_{\mu\nu}}{2} d_{\mu,\sigma}^{\alpha\dagger}(\mathbf{r}) d_{\nu,\sigma'}^{\alpha\dagger}(\mathbf{r}) d_{\mu,\sigma'}^{\alpha}(\mathbf{r}) d_{\nu,\sigma}^{\alpha}(\mathbf{r}) \\
& + \sum_{\mu < \nu} \sum_{\sigma, \sigma'} \frac{U'_{\mu\nu}}{2} d_{\mu,\sigma}^{\alpha\dagger}(\mathbf{r}) d_{\nu,\sigma'}^{\alpha\dagger}(\mathbf{r}) d_{\nu,\sigma'}^{\alpha}(\mathbf{r}) d_{\mu,\sigma}^{\alpha}(\mathbf{r}).
\end{aligned} \tag{7}$$

Here $\alpha \in \{A, B\}$, $\{\sigma, \sigma'\} \in \{\uparrow, \downarrow\}$ and $\{\mu, \nu\} \in \{yz, xz, xy\}$ label lattice sites, spins and orbitals, respectively. $d_{\mu,\sigma}^{\alpha\dagger}(\mathbf{r})$ and $d_{\mu,\sigma}^{\alpha}(\mathbf{r})$ are the second quantized operators creating and annihilating particles on sub-lattice A and B, see Fig.1(a). Using the results presented in Ref. 20 and assuming sharply localized Wannier functions of the xz , yz and xy orbitals, we can relate, up to a constant, the $d_{\mu,\sigma}^{\alpha}(\mathbf{k})$ operators acting in the one iron unit cell to the components of the doublets $\Psi_{X,\sigma}(\mathbf{k})$ and $\Psi_{Y,\sigma}(\mathbf{k})$ in the two iron unit cell via

$$d_{xz,\sigma}^{A(B)}(\mathbf{k}) \propto \pm \frac{1}{\sqrt{2}} c_{xz,\sigma}(\mathbf{k}), \tag{8}$$

$$d_{yz,\sigma}^{A(B)}(\mathbf{k}) \propto \frac{1}{\sqrt{2}} c_{yz,\sigma}(\mathbf{k}), \tag{9}$$

$$d_{xy,\sigma}^{A(B)}(\mathbf{k}) \propto \frac{1}{\sqrt{2}} (c_{xy,\sigma}^X(\mathbf{k}) \pm c_{xy,\sigma}^Y(\mathbf{k})), \tag{10}$$

where we absorb the constant prefactors into the Hubbard and Hund terms. As the xy orbital contributes to both X- and Y-point eq.(10) leads to "Umklapp" terms at the M-point.

We assume that even parity solutions are still the leading pairing instabilities (for odd parity solutions see Appendix B) and use Eqs.(8-10) to project eq.(7) onto the low energy model decoupled into the spin singlet A_{1g} s -wave and B_{2g} d -wave symmetry states which at the M-point in presence of inter-band SOC couple to the E_g even parity spin triplet state. When defining the two doublets $\Psi_{1\sigma}^T(\mathbf{k}) = (c_{yz\sigma}(\mathbf{k}), c_{xz\sigma}(\mathbf{k}))$ and $\Psi_{3\sigma}^T(\mathbf{k}) = (c_{xy^X\sigma}(\mathbf{k}), c_{xy^Y\sigma}(\mathbf{k}))$ the pairing terms read

$$\begin{aligned}
& H_{\text{int}}^{A_{1g}} + H_{\text{int}}^{B_{2g}} + H_{\text{int}}^{E_g} \\
& = \sum_{\mathbf{k}, \mathbf{q}} \left(\Psi_{1\uparrow}^{\dagger}(\mathbf{k}) \tau_0 \Psi_{1\downarrow}^*(-\mathbf{k}), \Psi_{3\uparrow}^{\dagger}(\mathbf{k}) \tau_0 \Psi_{3\downarrow}^*(-\mathbf{k}) \right) \times \\
& \quad \times \begin{pmatrix} \frac{1}{2}(U + J'_{11}) & J'_{13} \\ J'_{13} & U \end{pmatrix} \begin{pmatrix} \Psi_{1\downarrow}^T(-\mathbf{q}) \tau_0 \Psi_{1\uparrow}(\mathbf{q}) \\ \Psi_{3\downarrow}^T(-\mathbf{q}) \tau_0 \Psi_{3\uparrow}(\mathbf{q}) \end{pmatrix} \\
& + \frac{1}{2} \left[\Psi_{1\uparrow}^{\dagger}(\mathbf{k}) \tau_3 \Psi_{1\downarrow}^*(-\mathbf{k}) \right] (U - J'_{11}) \left[\Psi_{1\downarrow}^T(-\mathbf{q}) \tau_3 \Psi_{1\uparrow}(\mathbf{q}) \right] \\
& + \frac{1}{2} \left[\Psi_{1\sigma}^{\dagger}(\mathbf{k}) \tau_1 \Psi_{3\sigma}(-\mathbf{k}) \right] (U'_{13} - J_{13}) \left[\Psi_{3\sigma}^T(-\mathbf{q}) \tau_1 \Psi_{1\sigma}(\mathbf{q}) \right].
\end{aligned} \tag{11}$$

The 2x2 block in eq.(11) corresponds to A_{1g} s -wave pairing. We write $J'_{13} = \alpha J'_{11}$ and find two eigenvalues $E_{A_{1g}} = \frac{1}{4} \left(J'_{11} 2 + 3U \pm \sqrt{(J'_{11})^2 + \alpha 16 J'_{11} - 2 J'_{11} U + U^2} \right)$ which correspond to ordinary "plus-plus" (s^{++}) s -wave and sign-changing "plus-minus" (s^{\pm}) s -wave pairing, respectively. While the former channel is purely repulsive without spin-orbit coupling the latter becomes attractive once $J'_{11} > (U + U\sqrt{1+8\alpha})/4\alpha$.

The paring term that leads to B_{2g} d -wave is $E_{B_{2g}} = \frac{1}{2}(U - J'_{11})$ and can be directly read off. It is attractive once $J'_{11} > U$ and competes with sign-changing s -wave. Since we assume sharply located Wannier functions which yields eqs.(8-10) and on-site interactions only we find that within our simple mean field approximation the xy orbitals do not contribute to d -wave pairing as no "pair-hopping" term J'_{33} mediates between xy^X and xy^Y . This changes once the higher-order diagrams (spin fluctuations) are taken into account.

The E_g even parity spin triplet corresponds to pairing between the first (second) component of $\Psi_{X\sigma}(\mathbf{k})$ ($\Psi_{Y\sigma}(\mathbf{k})$) and the second (first) component of $\Psi_{Y\sigma}(\mathbf{k})$ ($\Psi_{X\sigma}(\mathbf{k})$) and is thus inter-band and attractive once $E_{E_g} = U'_{13} - J_{13} < 0$.

We perform a mean-field decoupling of Eq.(11) into A_{1g} and B_{2g} spin singlet channels with the pairing terms given by

$$A_{1g}^s : \Delta_1^A \Psi_{1,\sigma}^T(-\mathbf{k}) \tau_0 i\sigma^y \Psi_{1,\sigma'}(\mathbf{k}) \quad (12)$$

$$\Delta_3^A \Psi_{3,\sigma}^T(-\mathbf{k}) \tau_0 i\sigma^y \Psi_{3,\sigma'}(\mathbf{k}) \quad (13)$$

$$B_{2g}^s : \Delta_1^B \Psi_{1,\sigma}^T(-\mathbf{k}) \tau_3 i\sigma^y \Psi_{1,\sigma'}(\mathbf{k}) \quad (14)$$

$$\Delta_3^B \Psi_{3,\sigma}^T(-\mathbf{k}) \tau_3 i\sigma^y \Psi_{3,\sigma'}(\mathbf{k}). \quad (15)$$

In terms of $\Psi_{M,\sigma}(\mathbf{k})$ a triplet term can be written as $\Psi_{M,\sigma}^T(-\mathbf{k}) \hat{\mathcal{M}} i\sigma^y \sigma \Psi_{M,\sigma}(\mathbf{k})$, where $\hat{\mathcal{M}}$ and $i\sigma^y \sigma$ represent orbital and spin part, respectively. Since $i\sigma^y \sigma$ is symmetric an even (odd) parity triplet requires $\hat{\mathcal{M}}$ to be anti-symmetric (symmetric). $i\sigma^y \sigma$ can be divided into an in plane $i\sigma^y(\sigma^x, \sigma^y)$ and out of plane $i\sigma^y \sigma^z$ component which transform as the two dimensional E_g and one dimensional A_{2g} irreducible representation, respectively. In presence of SOC, orbital and spin degrees of freedom transform together under operations of the space group. We focus on the E_g even parity spin triplet that together with the E_g in-plane spin component decomposes into a direct sum of one dimensional representations as $E_g \otimes E_g = A_{1g} \oplus B_{1g} \oplus B_{2g} \oplus A_{2g}$. Using the two anti symmetric components of E_g and $\tau_{\pm} = (\tau_1 \pm i\tau_2)/2$

$$E_{g1}^- = i \begin{pmatrix} & \tau_- \\ -\tau_+ & \end{pmatrix} \quad E_{g2}^- = i \begin{pmatrix} & \tau_+ \\ -\tau_- & \end{pmatrix} \quad (16)$$

one finds two even parity spin triplets that transform according to A_{1g} and B_{2g} and hence, couple to the singlet channel.

$$A_{1g}^t : \Delta_t^A \Psi_{M,\sigma}^T(-\mathbf{k}) (-E_{g1}^-, iE_{g2}^-)(\sigma^z, \sigma_o) \Psi_{M,\sigma}(\mathbf{k}) \quad (17)$$

$$B_{2g}^t : \Delta_t^B \Psi_{M,\sigma}^T(-\mathbf{k}) (-E_{g1}^-, -iE_{g2}^-)(\sigma^z, \sigma_o) \Psi_{M,\sigma}(\mathbf{k}) \quad (18)$$

We refer the reader to Refs.^{21,32} for further details.

In terms of the spinor $\Psi_g^T(\mathbf{k}) = (\Psi_{X\uparrow}(\mathbf{k}), \Psi_{Y\downarrow}(\mathbf{k}), \Psi_{X\downarrow}^\dagger(\mathbf{k}), -\Psi_{Y\uparrow}^\dagger(\mathbf{k}))$ the BdG-Hamiltonian reads

$$H_{BdG}^{A_{1g}(B_{2g})} = \sum_{\mathbf{k}} \Psi_g^\dagger(\mathbf{k}) \begin{pmatrix} \mathcal{H}_0(\mathbf{k}) & \hat{\Delta}_{A_{1g}(B_{2g})} \\ \hat{\Delta}_{A_{1g}(B_{2g})}^\dagger & -\mathcal{H}_0(\mathbf{k}) \end{pmatrix} \Psi_g(\mathbf{k}) \quad (19)$$

with

$$\mathcal{H}_0(\mathbf{k}) = \begin{pmatrix} h_X^{\uparrow\uparrow}(\mathbf{k}) & \lambda_{\text{SOC}} \Lambda \\ \lambda_{\text{SOC}} \Lambda^\dagger & h_Y^{\downarrow\downarrow}(\mathbf{k}) \end{pmatrix}, \quad \Lambda = \begin{pmatrix} 0 & i \\ 1 & 0 \end{pmatrix} \quad (20)$$

and the pairing terms

$$\hat{\Delta}_{A_{1g}} = \begin{pmatrix} \Delta_1^A & & & -i\Delta_t^A \\ & \Delta_3^A & -\Delta_t^A & \\ & -\Delta_t^A & \Delta_1^A & \\ i\Delta_t^A & & & \Delta_3^A \end{pmatrix}, \quad (21)$$

$$\hat{\Delta}_{B_{2g}} = \begin{pmatrix} \Delta_1^B & & & i\Delta_t^B \\ & \Delta_3^B & -\Delta_t^B & \\ & -\Delta_t^B & -\Delta_1^B & \\ -i\Delta_t^B & & & -\Delta_3^B \end{pmatrix}. \quad (22)$$

where the gaps in orbital space are given by the equations (A1) and (A2). We self-consistently compute $\hat{\Delta}_{A_{1g}}$ and $\hat{\Delta}_{B_{2g}}$ as a function of temperature and inter-band SOC for the two cases $E_{A_{1g}} < E_{B_{2g}}$ and $E_{A_{1g}} > E_{B_{2g}}$ and present

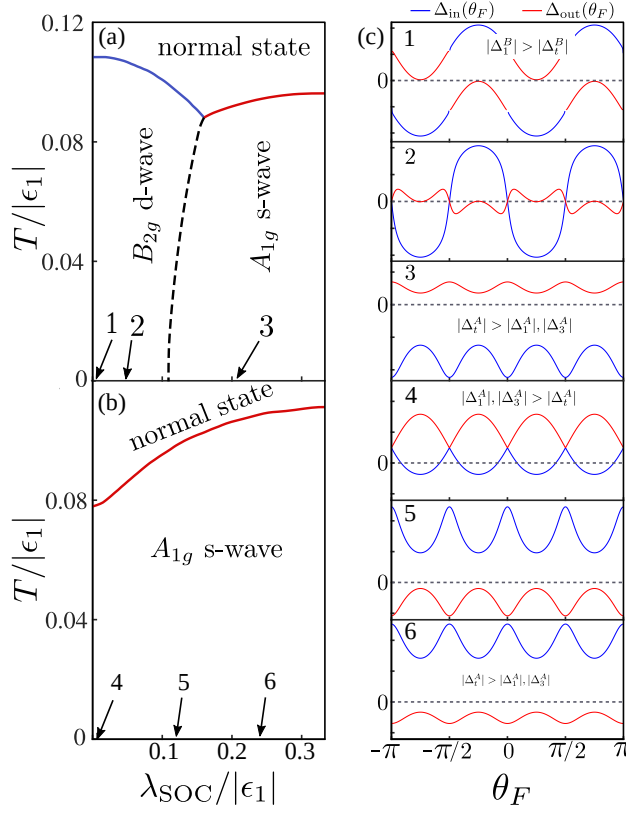


FIG. 2. Phase diagram as function of temperature and inter-band SOC in units of $|\epsilon_1|$. $\epsilon_1 = -45$ meV and $\epsilon_2 = -95$ meV are energies at the M-point of the two regular and the two incipient bands, respectively. The dimensionless coupling constants ($\tilde{U} = N_0 U$ etc. with $N_0 = \frac{2|m\mathbf{l}|}{2\pi}$) are for (a) $\tilde{U} = 0.5$, $\tilde{J}'_{11} = 2.58$, $\tilde{J}'_{13} = 0.83\tilde{J}'_{11}$, $\tilde{U}' = 0.1$ and $\tilde{J} = 4.6$ and for (b) $\tilde{U} = 0.5$, $\tilde{J}'_{11} = 2.58$, $\tilde{J}'_{13} = \tilde{J}'_{11}$, $\tilde{U}' = 0.1$ and $\tilde{J} = 4.6$. c) Superconducting gap projected on the inner (blue) and outer (red) Fermi-surface as function of the Fermi angle, zero temperature and at three different values of λ_{SOC} .

the phase diagrams in Fig.2(a) and Fig.2(b), respectively. Figure2(c) shows the angular dependence of the superconducting gap projected onto inner (blue) and outer (red) Fermi surface for three values of λ_{SOC} marked by black arrows. The gap projected on the l 'th band is given by $\Delta_l(\mathbf{k}) = \sum_{\alpha,\beta} \mu_{l\alpha}^\dagger(\mathbf{k}) \hat{\Delta}_{\alpha\beta} \mu_{\beta l}(\mathbf{k})$ where $\hat{\mu}(\mathbf{k})$ diagonalizes $\mathcal{H}_0(\mathbf{k})$.

In the case when solely $E_{A_{1g}}$ ($E_{B_{2g}}$) is attractive, Δ_t^A (Δ_t^B) is induced by SOC and scales with λ_{SOC} . In this case $|\Delta_t^{A(B)}| < |\Delta_1^{A(B)}|, |\Delta_3^{A(B)}|$ and we call the state a *spin singlet dominated* A_{1g} (B_{2g}). If E_{E_g} is attractive, however, Δ_t can develop independently of $\Delta_{1,3}$ and allows for states where $|\Delta_t^{A(B)}| > |\Delta_1^{A(B)}|, |\Delta_3^{A(B)}|$ which we call *spin triplet dominated* A_{1g} (B_{2g}). Equally whether the system is in the singlet or triplet dominated regime, the form of Eqs. (21) and (22) stays the same.

Depending on the ratio $\alpha = J'_{11}/J'_{13}$ the leading pairing symmetry for low values of λ_{SOC} is either B_{2g} d-wave or A_{1g} s-wave with accidental nodes and a sign change between inner and outer Fermi pocket. In Fig.2(a) we show a SOC mediated transition from B_{2g} d-wave to A_{1g} s-wave. For small values of λ_{SOC} we find a nodeless d-wave state where the nodes are lifted and the gap is opened by a combination of spin singlet and triplet components with the singlet gap being dominant $|\Delta_t^B| > |\Delta_1^B|$. With increasing λ_{SOC} the pairing symmetry changes from nodeless to nodal d-wave and finally to nodeless s-wave with a dominant inter-band triplet component $|\Delta_t^A| > |\Delta_1^A|, |\Delta_3^A|$. In Fig.2(b) we choose parameters such that the initial state at small λ_{SOC} is A_{1g} s-wave and has a dominant singlet gap $|\Delta_1^A| > |\Delta_t^A|$. Increasing λ_{SOC} lifts the nodes at the Fermi level and drives the system in an A_{1g} s-wave symmetry with a dominant triplet gap $|\Delta_t^A| > |\Delta_1^A|, |\Delta_3^A|$. We find that for large inter-band SOC the triplet dominated s-wave state wins over triplet dominated d-wave. The presence of an intra-band SOC term λ_z does not change the phase diagram qualitatively. However, in the region where λ_{SOC} is strong superconductivity in the d-wave channel is suppressed if $\lambda_z > 0$ which further stabilizes the A_{1g} -wave solution. Moreover, a large triplet gap, in addition to SOC, lifts accidental nodes leading to a nodeless s^\pm pairing symmetry.

Figure 2(a) is consistent with the phase diagram of phenomenological model in Ref. 14 with several important differences. In particular, in our model the singlet dominated d-wave state competes with singlet dominated bonding anti-bonding s^\pm which arises from pair hopping between $xz(yz)$ and xy orbitals. Furthermore, with increasing spin-orbit coupling strength the A_{1g} state contains dominant interband spin triplet component which was absent in the simplified analysis of Ref. 14 as its pairing channel turned out to be strongly repulsive in the two band model. Since SOC couples even parity inter-band triplet to intra-band even parity spin singlet pairing, an attraction in the former induces a gap in the latter channel and vice versa. Consequently a gap at the FS opens even though the E_g triplet is inter-band. A similar pairing state with attraction in the triplet channel was recently proposed for highly doped systems with only hole pockets³³.

IV. QUASIPARTICLE INTERFERENCE

A. Local density of states in presence of impurities

In order to investigate the QPI signatures of the possible pairing states we need to calculate the local density of states (LDOS) for a multi-orbital system in the superconducting state. We further investigate corrections to the LDOS which arise from scattering at single charge impurities to make a statement whether there is a sign-change between inner and outer electron pocket using HAEM's method. Moreover, we consider scattering from a single magnetic impurity to reveal information about the spin structure in the system.

In order to describe superconductivity and spin-resolved STM we introduce the 16 component Balian-Werthammer spinor

$$\Psi_{\mathbf{k}}^\dagger = \left(\Psi_{M,\uparrow}^\dagger(\mathbf{k}), \Psi_{M,\downarrow}^\dagger(\mathbf{k}), \Psi_{M,\downarrow}^T(-\mathbf{k}), -\Psi_{M,\uparrow}^T(-\mathbf{k}) \right). \quad (23)$$

Within this basis the Hamiltonian in the superconducting state is given by

$$H = \frac{1}{2} \sum_{\mathbf{k}} \Psi^\dagger(\mathbf{k}) \begin{pmatrix} \mathcal{H}(\mathbf{k}) & \hat{\Delta} \\ \hat{\Delta}^\dagger & -\mathcal{H}(\mathbf{k}) \end{pmatrix} \Psi(\mathbf{k}), \quad (24)$$

where the additional factor of $\frac{1}{2}$ accounts for double counting and

$$\mathcal{H}(\mathbf{k}) = \begin{pmatrix} h_X^{\uparrow\uparrow}(\mathbf{k}) & & & \Lambda \\ & h_Y^{\uparrow\uparrow}(\mathbf{k}) & -\Lambda^T & \\ & -\Lambda^* & h_X^{\downarrow\downarrow}(\mathbf{k}) & \\ \Lambda^\dagger & & & h_Y^{\downarrow\downarrow}(\mathbf{k}) \end{pmatrix}. \quad (25)$$

From Eq.(24) we find the superconducting Green's function $\hat{G}_{\mathbf{k}}^0(\omega) = [(\omega + i\delta)\mathbb{1}_{16 \times 16} - H_{BdG}(\mathbf{k})]^{-1}$ and the local density of states (LDOS) given by

$$\rho(\omega) = -\frac{1}{\pi} \text{Im} \sum_{\mathbf{k}} \text{Tr} \frac{\tau_1 + \tau_3}{2} \hat{G}_{\mathbf{k}}^0(\omega), \quad (26)$$

where we assumed sharply localized Wannier functions of the xz , yz and xy orbitals.

We now introduce a single on-site non-magnetic potential scatterer to the system which is located on either sublattice A or B. In the one-iron unit cell it can be described as

$$H_{\text{imp}}^{1Fe}(\mathbf{k}, \mathbf{k}') = V_{\alpha,\beta} d_{\alpha,\sigma}^\dagger(\mathbf{k}) d_{\beta,\sigma}^A(\mathbf{k}'). \quad (27)$$

We assume that the major contribution to scattering is of intra-orbital nature and project eq.(27) onto the states in the two iron unit cell. Due to the fact that $d_{xy}^{A/B}$ in the projected model is a linear combination of c_{xy^X} and c_{xy^Y} the intra-orbital term induces scattering between xy^X and xy^Y thus also contributes to inter-band scattering. In the two iron unit cell the impurity potential is given by

$$H_{\text{imp}}^{2Fe}(\mathbf{k}, \mathbf{k}') = \Psi_{M,\sigma}^\dagger \tilde{V} \Psi_{M,\sigma} \quad (28)$$

with

$$\tilde{V} = \begin{pmatrix} V_{yz,yz} & & \\ & V_{xy^X,xy^X} & V_{xy^X,xy^Y} \\ & & V_{xz,xz} \\ & V_{xy^X,xy^Y} & V_{xy^Y,xy^Y} \end{pmatrix}. \quad (29)$$

Following the HAEM²⁴ approach, we compute the antisymmetrized correction to the LDOS due to impurity scattering

$$\delta\rho^-(\omega) = \delta\rho(\omega) - \delta\rho(-\omega), \quad (30)$$

$$\delta\rho(\omega) = -\frac{1}{2\pi} \text{ImTr} \frac{\tau_0 + \tau_3}{2} \sigma^0 \sum_{\mathbf{q}} \delta\hat{G}_{\mathbf{q}}(\omega), \quad (31)$$

with $\delta\hat{G}_{\mathbf{q}}(\omega) = \sum_{\mathbf{k}} \hat{G}_{\mathbf{k}}^0(\omega) \hat{U} \hat{G}_{\mathbf{k}+\mathbf{q}}^0(\omega)$ being the convolution of the bare Green's functions dressed by a Nambu scattering matrix $\hat{U} = \tau_3 \otimes \sigma_0 \otimes \tilde{V}$ in Born approximation, i.e. with $V_{\alpha,\beta} \ll E_F$, where E_F is the Fermi energy.

The HAEM method states that the momentum integrated and antisymmetrized LDOS, $\delta\rho^-(\omega)$, qualitatively differs in case of a sign-changing OP from that of a sign-preserving one yielding a strong enhancement of the integrated response for the sign-changing but not the sign-preserving one. This method has been recently successfully applied to confirm the sign-changing nature of the order parameter in FeSe²⁷, where the superconducting gaps are also extremely anisotropic. More recently, the method has also been applied to $(\text{Li}_{1-x}\text{Fe}_x)\text{OHFe}_{1-y}\text{Zn}_y\text{Se}$ ²⁸ where $\delta\rho^-(\omega)$ shows a strong signal and no sign-change between 8 meV and 14 meV suggesting a sign-changing s^\pm pairing symmetry. Since our previous analysis shows that most of the conclusions regarding the phase structure of the superconducting gap obtained within Born limit are robust and remain valid also well beyond this limit, we restrict our analysis to weak potential scatterers.

B. Local density of states and phase sensitive correction to QPI

We would like to discuss singlet and triplet dominated A_{1g} - and B_{2g} -wave with respect to their consistency with QPI experiments in $(\text{Li}_{1-x}\text{Fe}_x)\text{OHFe}_{1-y}\text{Zn}_y\text{Se}$. Recently in Ref.(21) possible pairing states for intercalated FeSe have been discussed. Following Ref.[21] the pairing has to obey three criteria in order to be consistent with experiments: i) fully gaped LDOS, ii) the quasiparticle energy extrema are at or close to k_F of the normal state ("back bending") and iii) two peak features in the DOS with a peak at about 8 meV and 14 meV, respectively. In the context of monolayer and intercalated FeSe it has been suggested that the second peak in the DOS arises due to pure interband gap²¹ as in the former the gap size seen by ARPES¹⁶ (13.7 meV) significantly deviates from the peak energy (20.1 meV) seen by STM⁸. This, however, does not have to be the case with the electron-intercalated materials where a gap of 13 ± 2 meV around the Fermi energy was reported¹⁰. Three pairing states were proposed to be consistent with experimental data. These are A_{1g} s -wave and B_{2g} d -wave and $E_u \otimes U(1)$ helical p -wave. The A_{1g} and B_{2g} state were assumed to have a dominant intra-band singlet gap in order to ensure a full gap and back bending. An inter-band SOC then mixes in inter-band triplet E_g pairing. For the odd parity intra-band triplet $E_u \otimes U(1)$ p -wave state its the odd parity inter-band singlet A_{2u} that is coupled via SOC.

In the following we investigate spin singlet and spin triplet dominated A_{1g} - and B_{2g} -wave for their consistency with the criteria i)-iii) and the QPI data. For that we use Eq.(24) and calculate the LDOS ($\rho(\omega)$) and the superconducting band dispersion to ensure i)-iii) are fulfilled. In addition, for each pairing state, we calculate the antisymmetrized correction to the LDOS ($\delta\rho^-(\omega)$) to check whether the order parameter changes sign between electron pockets. Since the gaps in the intercalated FeSe are found to be isotropic¹⁰ we further present the angular dependence of the gap projected on the inner and outer electron pocket, respectively. In Appendix (B) we also briefly discuss the QPI data for the odd parity E_u -wave state and show that at least within Born scattering the results are not compatible with experiment.

We find that A_{1g} and B_{2g} states with a dominant spin triplet gap can show back bending *and*, in contrast to their

singlet dominated states and the odd parity E_u -state, give an appropriate description of the QPI data found in experiment.

One should also further note that for the HAEM method the crucial role is played by the gaps present on the Fermi surface pockets. In the present case there is also additional interband gap. We show in the Appendix C that its phase structure with respect to the gaps present on the Fermi level cannot be elucidated within phase-sensitive QPI analysis. Furthermore, we show that the sign-changing and sign-preserving gaps on the Fermi surface still determine the characteristic features of $\delta\rho^-(\omega)$.

C. A_{1g} -symmetry state

We start by examining spin singlet and triplet dominated s -wave pairing state. We use the singlet gaps Δ_1 and Δ_3 and the triplet gap Δ_t to fit band-structure and LDOS.

1. Spin-singlet dominated A_{1g} -wave state

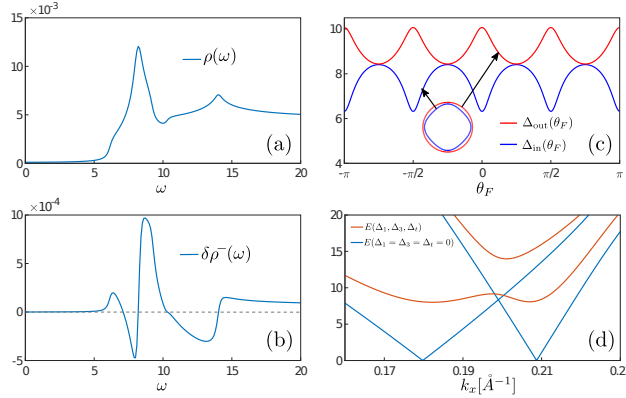


FIG. 3. Figures calculated from equation (24) for singlet dominated A_{1g} and (in meV) $\epsilon_1 = -45$, $\epsilon_3 = -95$, $\Delta_1 = 10.8$, $\Delta_3 = 7.2$, $\Delta_t = -3$ and $\lambda_{\text{SOC}} = 5$.

(a) $\rho(\omega)$ fully gaped, with peaks at 8 meV and 14 meV. (b) $\delta\rho^-(\omega)$ for charge impurity in Born limit. Sign-change in $\delta\rho^-(\omega)$ between 6 meV and 10 meV indicates that there is no sign change of OP between inner and outer pocket. (c) Gap projected on inner (blue) and outer (red) electron pocket as function of the Fermi angle θ_F . (d) Orange: Positive branches of upper and lower superconducting bands in ΓM -direction. Blue: Same bands for zero gap. The lower orange band has its minima centered above the former Fermi-level "back-bending".

To start with singlet dominated s -wave we utilize the fitting parameters presented in Ref. 21. As shown in Fig.3(a), $\rho(\omega)$ is indeed fully gaped and has a peak at 8 meV and 14 meV. The first peak between 6 – 10 meV mostly comes from the intra-band gaps at the electron pockets as can be seen by comparison with the gap projections on the inner, Δ_{in} and outer, Δ_{out} , electron pocket, Fig.3(c). At $\theta_F = \pi/4$ both gaps are equal in magnitude leading to a peak at $\omega \sim 8$ meV in $\rho(\omega)$. The width of the peak is limited by 6 meV and 10 meV which correspond to the minimum of Δ_{in} and the maximum of Δ_{out} , respectively, so that the occupied states below and above 8 meV are due to anisotropy of the gaps. The second peak at 14 meV is indeed due to inter-band pairing. It vanishes for $\lambda_{\text{SOC}} \rightarrow 0$ and $\Delta_t \rightarrow 0$. We find that both gaps are highly anisotropic and most important positive on both Fermi surface pockets, yielding an s^{++} -pairing symmetry. In Fig.3(b) $\delta\rho^-(\omega)$ exhibits a sign change in the region $6 \text{ meV} < \omega < 10 \text{ meV}$ which can be interpreted as a sign preserving order parameter and thus is not compatible with the QPI data²⁸. Note that this state does not appear in our phase diagram, shown in Fig.2, where the A_{1g} state is sign-changing. The feature at $\omega \sim 14$ meV in $\delta\rho^-(\omega)$ for this state appears due to the small inter-band contribution and does not carry phase information as we explain for a simple model in Appendix C. In Fig.3(d) the superconducting band dispersion in ΓM -direction ($\theta_F = \pi/4$) is shown where the minima of the lower superconducting band are located above the former Fermi level (back-bending).

It turns out that the fitting parameters for spin singlet dominated s -wave, proposed in Ref. 21 would give rise to s^{++} superconductivity. A possible s^\pm pairing symmetry with a dominant spin singlet gap, on the contrary, would require $\text{sign}\Delta_1^A \neq \text{sign}\Delta_3^A$. This state in our analysis exhibits highly anisotropic gaps and possible accidental nodes

(see for example Fig.2c(1)). This makes it difficult to fit the U-shaped two peaked LDOS in the LiOH-intercalated FeSe data without invoking a spin triplet component, induced by spin-orbit coupling that lifts the nodes.

2. Spin-triplet dominated A_{1g} -wave state

In Fig.4(a) and Fig.4(d) the LDOS and the superconducting band dispersion are shown. The LDOS shows a full gap and a peak at 8 meV and 13.7 meV, respectively, while the lower superconducting band shows back bending. The band projected gaps Δ_{in} and Δ_{out} we plot in Fig.4(c). Possible accidental nodes are lifted by a large Δ_t leading to a nodeless s^\pm pairing symmetry with two almost isotropic gaps. In Fig.4(b) we present $\delta\rho^-(\omega)$ which in contrast to the singlet dominated case does not change sign between 8 meV and 14 meV. If we compare Fig.4(a) and Fig.4(c) we find that the peak positions of the two peaks roughly agree with the the magnitudes of Δ_{in} and Δ_{out} and thus $\delta\rho^-(\omega)$ and the behavior of $\delta\rho^-(\omega)$ agrees with the experimental one. The first peak is sharper than the second since Δ_{in} is very isotropic. The second peak is broader as a consequence of an anisotropic Δ_{out} and the contribution from inter-band pairing. In contrast to the singlet dominated case $\delta\rho^-(\omega)$ exhibits well pronounced negative peaks at $\omega_1 \approx \Delta_{out}$ and $\omega_2 \approx \Delta_{in}$ without a sign change between them indicating an OP that changes sign between the electron pockets consistent with the experimental QPI data and ARPES data^{10,28}. Also note that for the spin triplet dominated A_{1g} state the direct gap feature caused by Δ_{out} is very close to the interband feature in the DOS which agrees with the findings in Ref.10 and 28.

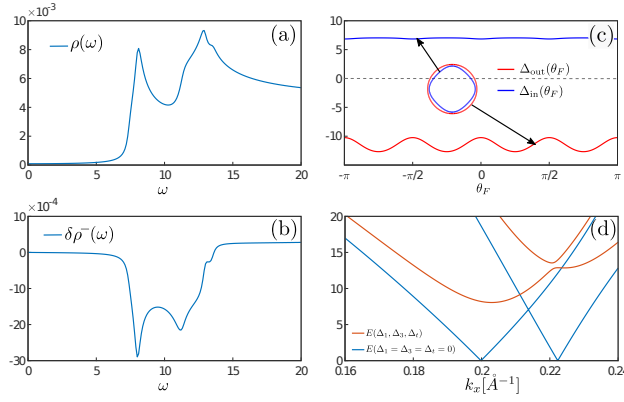


FIG. 4. Figures calculated from equation (24) triplet dominated A_{1g} and (in meV) $\epsilon_1 = -55$, $\epsilon_3 = -105$, $\Delta_1 = 6.75$, $\Delta_3 = -6.03$, $\Delta_t = 10.27$ and $\lambda_{SOC} = 7.5$. (a) refer to $\rho(\omega)$ fully gaped, with peaks at 8 meV and 13.7 meV. (b) $\delta\rho^-(\omega)$ for charge impurity in Born limit. No sign-change of $\delta\rho^-(\omega)$ between 8 meV and 13.7 meV indicates an OP changing sign between inner and outer pocket. (c) Gap projected on inner (blue) and outer (red) electron pocket as function of the Fermi angle θ_F . (d) Orange: Positive branches of upper and lower superconducting bands, in ΓM -direction. Blue: Same bands for zero gap. The lower orange band has its minima centered above the former Fermi-level "back-bending".

D. B_{2g} -symmetry state

We now discuss the singlet and triplet dominated B_{2g} d -wave pairing state. We use the singlet gaps Δ_1 and Δ_3 and the triplet gap Δ_t to fit band structure and LDOS. Note that even though our simple mean field approach leads to $\Delta_3 = 0$ for the d -wave case, as it involves decoupling of the repulsive intraorbital Hubbard interaction, a nonzero Δ_3 is necessary to achieve qualitative agreement when fitting the experimental data. In theoretical calculations, a nonzero Δ_3 appears due to inclusion of the spin fluctuation diagrams in the Cooper-pairing channel yielding momentum dependent interaction, see Ref. 11.

1. Spin-singlet dominated B_{2g} -state

For the spin singlet dominated B_{2g} -wave state appropriate fitting parameters were found in Ref.(21). As shown in Fig.5(a) and Fig.5(d) the LDOS is fully gaped and has a peak at 8 meV and 14 meV, moreover, the lower superconducting band shows back bending. Δ_{in} and Δ_{out} are plotted in Fig.5(c). Both gaps are almost equal in

magnitude and nodeless due to smallness of hybridization between the electron pockets, i.e. $|\Delta_{in/out}| > \lambda_{SOC}$. The first peak in the LDOS is due to the intra-band gaps Δ_{in} and Δ_{out} . We calculate $\delta\rho^-(\omega)$ and present the results in Fig.5(b). $\delta\rho^-(\omega)$ has positive peaks at ~ 7 meV and ~ 9 meV with no sign change between them indicating the sign change between Δ_{in} and Δ_{out} . Yet the third peak at ~ 14 meV comes from inter-band pairing and causes two sign changes between second and third peak which is at odds with the experimental data²⁸.

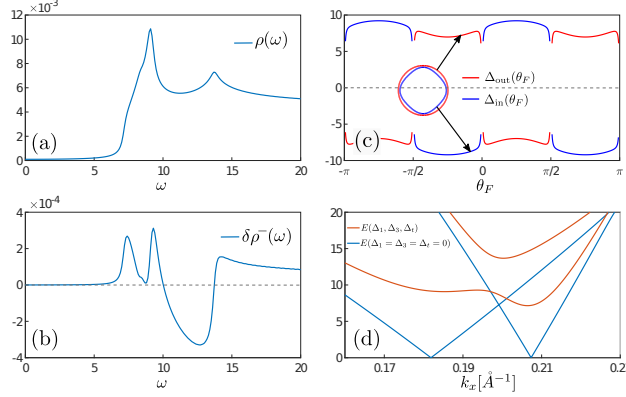


FIG. 5. Figures calculated from equation (24) for singlet dominated B_{2g} and (in meV) $\epsilon_1 = -45$, $\epsilon_3 = 95$, $\Delta_1 = 10.8$, $\Delta_3 = 7.2$, $\Delta_t = -4.8$ and $\lambda_{SOC} = 0.5$.

(a) $\rho(\omega)$ fully gaped with two peaks at 8 meV and 14 meV. (b) $\delta\rho^-(\omega)$ for charge impurity in Born limit. No sign-change between 6 meV and 10 meV indicates OP changes sign between inner and outer pocket. (c) Gap projected on inner (blue) and outer (red) electron pocket as function of the Fermi angle θ_F . (d) Orange: Positive branches of upper and lower superconducting bands, in ΓM -direction. Blue: Same bands for zero gap. The lower orange band has its minima centered above the former Fermi-level "back-bending".

2. Spin-triplet dominated B_{2g} -state

Even though a triplet dominated d -wave scenario is not realized in the phase diagram we quickly discuss this case with respect to criteria i)-iii) and QPI data.

As shown in Fig.6(a) and Fig.6(d) the LDOS is fully gaped and has a peak at 8 meV and 14 meV, moreover, the lower superconducting band shows back bending. Δ_{in} and Δ_{out} are plotted in Fig.6(c). Both gaps are equal in magnitude and nodeless due to smallness of hybridization between the electron pockets. In contrast to the singlet dominated case for the triplet dominated case we use $|\Delta_t^B| > |\Delta_{1/3}^B|$ and $\text{sign}(\Delta_t^B) = \text{sign}(\Delta_1^B) = \text{sign}(\Delta_2^B)$. In Fig.6(b) we plot $\delta\rho^-(\omega)$. Two small peaks between 7 meV and 8 meV reflect Δ_{in} and Δ_{out} contributions to $\delta\rho^-(\omega)$. The peak at 15 meV is due to the large inter-band gap. Overall, the behavior of $\delta\rho^-(\omega)$ is nearly consistent with experimental data as $\delta\rho^-(\omega)$ does not change sign in the experimentally relevant energy range. However, one has to bear in mind that in contrast to the triplet driven A_{1g} case the phase structure of the gaps on the Fermi surface affect the behavior of $\delta\rho^-(\omega)$ only near the lower peak, and the structure near the second (interband) peak is determined by the interband gap and does not necessarily bear information about the signs of the order parameters (see Appendix C.2).

As we clearly see, to obtain the agreement with QPI experiments²⁸ the spin-triplet interband component from E_g state is necessarily required in both symmetry states and triplet dominated A_{1g} state appears most likely one. This poses an important question how to detect it. To stay within QPI we propose to employ spin-resolved STM as an additional tool to further specify the underlying pairing state and also to distinguish between B_{2g} and A_{1g} -states.

E. Spin resolved STM

In the previous section we investigated corrections to the LDOS which arise from scattering on a single non-magnetic charge impurity and found the triplet dominated A_{1g} and B_{2g} pairing states in the presence of SOC to be consistent with the available experiments. As discussed in the introduction, however, the more conventional spin singlet A_{1g} and B_{2g} states have also been proposed. This raises the question whether SOC effects and the spin triplet order

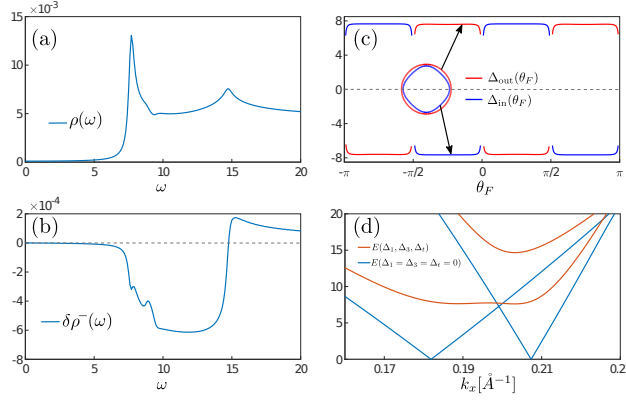


FIG. 6. Figures calculated from equation (24) for triplet dominated B_{2g} and (in meV) $\epsilon_1 = -45$, $\epsilon_3 = 95$, $\Delta_1 = 7.65$, $\Delta_3 = 7.2$, $\Delta_t = 9.37$ and $\lambda_{\text{SOC}} = 0.5$.

(a) $\rho(\omega)$ fully gaped with two peaks at 8 meV and 14 meV. (b) $\delta\rho^-(\omega)$ for charge impurity in Born limit. No sign-change between 6 meV and 8 meV indicates OP changes sign between inner and outer pocket. (c) Gap projected on inner (blue) and outer (red) electron pocket as function of the Fermi angle θ_F . (d) Orange: Positive branches of upper and lower superconducting bands, in ΓM -direction. Blue: Same bands for zero gap. The lower orange band has its minima centered above the former Fermi-level "back-bending".

parameter can be further verified in experiment. Here we propose spin-resolved QPI as an additional tool to further specify the underlying pairing state. To illustrate the possible capabilities of this technique, we study the corrections to the LDOS in Born approximation from a single magnetic impurity which, within our basis of eq.(23), is given by $\hat{U} = \tau_3 \otimes \sigma^z \otimes \hat{V}$. Here τ and σ matrices act on Nambu and spin-space, respectively, and the matrix \hat{V} describes orbital scattering. The Fourier transform of the spin resolved σ^i -projected correction to the LDOS is given by [34]

$$\begin{aligned} \delta\rho_{\sigma^i}(\mathbf{q}, \omega) &= -\frac{1}{2\pi i} \text{Tr} \frac{\tau_0 + \tau_3}{2} \sigma^i \left[\delta\hat{G}_{\mathbf{q}}(\omega) - \delta\hat{G}_{-\mathbf{q}}^*(\omega) \right] \\ &= -\frac{1}{2\pi} \text{Tr} \frac{\tau_0 + \tau_3}{2} \sigma^i \sum_{\mathbf{k}} \left[\text{Im} \left[G_{\mathbf{k}}(\omega) \hat{U} G_{\mathbf{k}+\mathbf{q}}(\omega) + G_{-\mathbf{k}}(\omega) \hat{U} G_{-\mathbf{k}-\mathbf{q}}(\omega) \right] \right. \\ &\quad \left. - i \text{Re} \left[G_{\mathbf{k}}(\omega) \hat{U} G_{\mathbf{k}+\mathbf{q}}(\omega) - G_{-\mathbf{k}}(\omega) \hat{U} G_{-\mathbf{k}-\mathbf{q}}(\omega) \right] \right], \end{aligned} \quad (32)$$

with the real and the imaginary part being even and odd in \mathbf{q} , respectively. Note that a non-vanishing imaginary part requires the scattering potential to break inversion symmetry, which, as we show below can result from interorbital scattering. The scattering matrix $\hat{V} = \hat{V}_z + \hat{V}_x$ can be written as

$$\hat{V} = \begin{pmatrix} V_{yz,yz}^{\text{intra}} & V_{yz,xy^X}^{\text{inter}} \\ V_{yz,xy^X}^{\text{inter}} & V_{xy^X,xy^X}^{\text{intra}} \\ & & V_{xz,xz}^{\text{intra}} & V_{xz,xy^Y}^{\text{inter}} \\ & & V_{xz,xy^Y}^{\text{inter}} & V_{xy^Y,xy^Y}^{\text{intra}} \end{pmatrix} + \begin{pmatrix} & & V_{yz,xz}^{\text{inter}} & V_{yz,xy^Y}^{\text{inter}} \\ & & V_{xy^X,yz}^{\text{inter}} & V_{xy^X,xy^Y}^{\text{intra}} \\ V_{yz,xy^Y}^{\text{inter}} & V_{xy^X,xz}^{\text{inter}} & & \\ V_{xz,xy^Y}^{\text{inter}} & V_{xy^X,xy^Y}^{\text{intra}} & & \end{pmatrix}. \quad (33)$$

where, in Born approximation, \hat{V}_z potentially contributes to the σ^z - and \hat{V}_x to the $\sigma^{x(y)}$ -polarized LDOS when taking the trace in eq.(32). The labels intra and inter denote intra- and interorbital scattering, respectively. Note that in each block of the matrices \hat{V}_z (\hat{V}_x) it is the off-diagonal (diagonal) elements that break inversion symmetry since under inversion $\Psi_X(-\mathbf{k}) = \sigma^z \Psi_X(\mathbf{k})$ and $\Psi_Y(-\mathbf{k}) = -\sigma^z \Psi_Y(\mathbf{k})$. Those elements contribute to $\text{Im}\delta\rho_{\sigma^i}(\mathbf{q}, \omega)$, while inversion symmetric ones contribute to $\text{Re}\delta\rho_{\sigma^i}(\mathbf{q}, \omega)$.

Results are presented in Fig.7 exemplary for $\omega = 8$ meV where we show real and imaginary part of $\delta\rho_{\sigma^i}(\mathbf{q}, \omega)$ as a function of the scattering vector \mathbf{q} for a σ^z impurity with $i = z$ (a-d) and $i = x$ (e-h). Note that a similar behavior of these quantities is found for all frequencies within the range of the two maxima in the LDOS at 8 meV and 14 meV, respectively.'

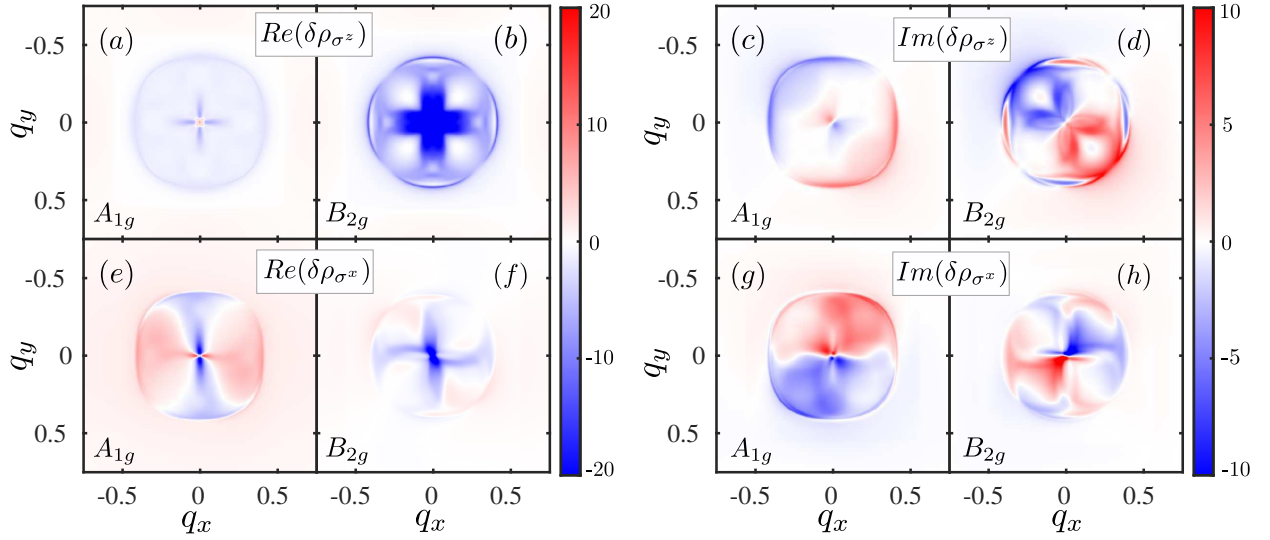


FIG. 7. Spin polarized correction to the LDOS for a magnetic impurity in Born limit. Real and imaginary part of $\delta\rho_{\sigma^z}(\mathbf{q}, \omega)$ (a-d) and $\delta\rho_{\sigma^x}(\mathbf{q}, \omega)$ (e-h) for triplet dominated A_{1g} and B_{2g} state at $\omega = 8$ meV.

In Fig.7.(a,b) $\text{Re}\delta\rho_{\sigma^z}$ shows an even in \mathbf{q} C_4 -symmetric QPI pattern qualitatively similar for the A_{1g} and B_{2g} pairing state. In contrast to that, see Fig.7.(c,d), $\text{Im}\delta\rho_{\sigma^z}$ is odd in \mathbf{q} and exhibit a few qualitative differences between A_{1g} and B_{2g} especially along the intensity edges. Note, however, that $\text{Im}\delta\rho_{\sigma^z}$ is caused by the inter-orbital terms in \hat{V}_z and hence is expected to show a weakened intensity if $V^{\text{inter}} \ll V^{\text{intra}}$.

In Fig.7.(e-h) we present real and imaginary part of the σ^x -polarized QPI pattern $\delta\rho_{\sigma^x}(\mathbf{q}, \omega)$. We would like to stress that this quantity is non-zero only in presence of either a triplet gap $\Delta_t^{A(B)}$ or SOC, which then itself induces a triplet gap. The same is true for the σ^y - polarized state which is related to $\delta\rho_{\sigma^x}(\mathbf{q}, \omega)$ by 90° rotation.

In Fig.7.(e-f) we show the real part $\delta\rho_{\sigma^x}$ which is C_2 -symmetric and even in \mathbf{q} while the imaginary part is odd, see Fig.7.(g,h). In contrast to $\delta\rho_{\sigma^z}$ the patterns for A_{1g} and B_{2g} representation show qualitative differences in both real and imaginary part. Moreover, if the impurity occupies one Fe site (either on sub lattice A or B) \hat{V}_x contains scattering between xy^X and xy^Y components which breaks inversion symmetry and according to eq.(10) is of intra-orbital nature. Hence, we expect the QPI signal of $\text{Im}\delta\rho_{\sigma^x}$ to be of the same order of magnitude as $\text{Re}\delta\rho_{\sigma^z}$ and hence may provide a quantity that allows to distinguish triplet driven A_{1g} from B_{2g} .

Thus we have shown that the spin-resolved QPI is a useful tool to study the details of the spin-orbit coupling and the triplet order parameter; our results suggest that a combination of spin-resolved QPI with the more conventional probes can be used to determine the symmetry as well as spin structure of pairing in iron-based superconductors.

V. CONCLUSION

In conclusion, we remind the reader that the highly electron-doped Fe-chalcogenides, in particular the $(\text{Li}_{1-x}\text{Fe}_x)\text{OHFeSe}$ system, have been discussed intensively in the context of the standard model of spin-fluctuation induced spin singlet pairing in the limit of weak spin-orbit coupling. In this case, the nodeless d -wave (B_{2g}) and bonding-antibonding s_{\pm} (A_{1g}) spin singlet states on the electron pockets have been considered most favorable, with the additional possibility of incipient s_{\pm} pairing via coupling to the incipient hole pocket at Γ . One of these states may eventually prove to be the correct pairing state for these materials, if the effective attraction in these channels generated by spin fluctuations driven by interpocket repulsion dominate the pair vertex¹¹.

Here, we have instead studied the new possibility raised previously²⁰, namely that interorbital triplet components generated by intrinsic attractions possible only in the presence of spin orbit coupling are responsible for the pairing in these systems. We explored the various possible Cooper-pairing symmetries using a mean-field decomposition of the Hubbard-Kanamori Hamiltonian including A_{1g} and B_{2g} states. For nonzero spin-orbit coupling, the superconducting order parameter is a combination of spin singlet and spin triplet gaps in each state. Treating attraction in singlet and triplet channels on equal footing and solving the self-consistency equations, we found for weak spin-orbit coupling a dominant spin singlet and small spin triplet gap yielding a state essentially equivalent to those identified in the usual spin fluctuation approach. For stronger spin-orbit coupling, however, the superconducting order parameter is a

combination of spin singlet and dominant spin triplet gaps in each state. Focusing on the $(\text{Li}_{1-x}\text{Fe}_x)\text{OHFeSe}$ system, we identified the even parity A_{1g} - and B_{2g} - pairing states with a dominant spin triplet component to be consistent with available experiments, including current quasiparticle interference data, whereby according to our phase-diagram the A_{1g} state is slightly favored. The spin-singlet dominated A_{1g} and B_{2g} -states in this scenario without strong spin fluctuations are not consistent with at least one of the existing experiments.

In summary, to obtain a full moderately anisotropic gap on the Fermi pockets and its sign-changing character in agreement with experimental results on $(\text{Li}_{1-x}\text{Fe}_x)\text{OHFeSe}$, we require *either* the traditional intraband A_{1g} or B_{2g} states generated by spin fluctuations, *or* the new triplet interband pair states in the same symmetry channels generated by intrinsic attraction in multiorbital correlated models. It is clearly of interest to identify experimental tests to distinguish between these possibilities. To this end we proposed using spin-polarized QPI to identify the possible triplet components present in the more exotic alternative states, and presented results for each of the triplet dominated states. A clear identification of triplet interband pairing using these results would be an important step forward in understanding the unusual superconductivity in the Fe chalcogenides.

ACKNOWLEDGMENTS

We thank P. M. Eugenio, O. Vafek, A. V. Chubukov and P. Coleman for useful discussions. J.B. and I.E. were supported by the joint DFG-ANR Project (ER 463/8-1) and DAAD PPP USA N57316180. P.J.H. was supported by the U.S. Department of Energy under Grant No. DE-FG02-05ER46236. P.A.V. acknowledges the support by the Rutgers University Center for Materials Theory Postdoctoral fellowship.

-
- ¹ K. Kuroki, S. Onari, R. Arita, H. Usui, Y. Tanaka, H. Kontani, and H. Aoki, Phys. Rev. Lett. **101**, 087004 (2008).
 - ² I. I. Mazin, D. J. Singh, M. D. Johannes, and M. H. Du, Phys. Rev. Lett. **101**, 057003 (2008).
 - ³ A. V. Chubukov, D. V. Efremov, and I. Eremin, Phys. Rev. B **78**, 134512 (2008).
 - ⁴ A. V. Chubukov, Annu. Rev. Condens. Matter Phys. **3**, 57 (2012).
 - ⁵ P. Hirschfeld, C. R. Phys. **17**, 197 (2016).
 - ⁶ J. Guo, S. Jin, G. Wang, S. Wang, K. Zhu, T. Zhou, M. He, and X. Chen, Phys. Rev. B **82**, 180520(R) (2010).
 - ⁷ X. Lu, N. Wang, H. Wu, Y. Wu, D. Zhao, X. Zeng, X. Luo, T. Wu, W. Bao, G. Zhang, F. Huang, Q. Huang, and X. Chen, Nature Materials **14**, 325 (2015).
 - ⁸ Q.-Y. Wang, Z. Li, W.-H. Zhang, Z.-C. Zhnag, J.-S. Zhang, W. Li, H. Ding, Y.-B. Ou, P. Deng, K. Chang, J. Wen, C.-L. Song, K. He, J.-F. Jia, S.-H. Ji, Y.-Y. Wang, L.-L. Wang, X. Chen, X.-C. Ma, and Q.-K. Xue, Chin. Phys. Lett. **29**, 037402 (2012).
 - ⁹ Y. Miyata, K. Nakayama, K. Sugawara, T. Sato, and T. Takahashi, Nature Mater **14**, 775 (2015).
 - ¹⁰ L. Zhao, A. Liang, D. Yuan, Y. Hu, D. Liu, J. Huang, S. He, B. Shen, Y. Xu, X. Liu, L. Yu, G. Liu, H. Zhou, Y. Huang, X. Dong, F. Zhou, K. Liu, Z. Lu, Z. Zhao, C. Chen, Z. Xu, and X. J. Zhou, Nature Commun. **7**, 10608 (2016).
 - ¹¹ T. A. Maier, S. Graser, P. J. Hirschfeld, and D. J. Scalapino, Phys. Rev. B **83**, 100515 (2011).
 - ¹² F. Wang, F. Yang, M. Gao, Z.-Y. Lu, T. Xiang, and D.-H. Lee, Europhys. Lett. **93**, 57003 (2011).
 - ¹³ I. I. Mazin, Phys. Rev. B **84**, 024529 (2011).
 - ¹⁴ M. Khodas and A. V. Chubukov, Phys. Rev. Lett. **108**, 247003 (2012).
 - ¹⁵ Y. J. Yan, W. H. Zhang, M. Q. Ren, X. Liu, X. F. Lu, N. Z. Wang, X. H. Niu, Q. Fan, J. Miao, R. Tao, B. P. Xie, X. H. Chen, T. Zhang, and D. L. Feng, Phys. Rev. B **94**, 134502 (2016).
 - ¹⁶ Y. Zhang, J. J. Lee, R. G. Moore, W. Li, M. Yi, M. Hashimoto, D. H. Lu, T. P. Devereaux, D.-H. Lee, and Z.-X. Shen, Phys. Rev. Lett. **117**, 117001 (2016).
 - ¹⁷ S. Onari and H. Kontani, Phys. Rev. Lett. **109**, 137001 (2012).
 - ¹⁸ P. J. Hirschfeld, M. M. Korshunov, and I. I. Mazin, Rep. Prog. Phys. **74**, 124508 (2011).
 - ¹⁹ A. Kreisel, Y. Wang, T. A. Maier, P. J. Hirschfeld, and D. J. Scalapino, Phys. Rev. B **88**, 094522 (2013).
 - ²⁰ V. Cvetkovic and O. Vafek, Phys. Rev. B **88**, 134510 (2013).
 - ²¹ P. M. Eugenio and O. Vafek, Phys. Rev. B **98**, 014503 (2018).
 - ²² T. Pereg-Barnea and M. Franz, Phys. Rev. B **68**, 180506 (2003).
 - ²³ T. S. Nunner, W. Chen, B. M. Andersen, A. Melikyan, and P. J. Hirschfeld, Phys. Rev. B **73**, 104511 (2006).
 - ²⁴ P. J. Hirschfeld, D. Altenfeld, I. Eremin, and I. I. Mazin, Phys. Rev. B **92**, 184513 (2015).
 - ²⁵ J. H. J. Martiny, A. Kreisel, P. J. Hirschfeld, and B. M. Andersen, Phys. Rev. B **95**, 184507 (2017).
 - ²⁶ S. Chi, W. Hardy, R. Liang, P. Dosanjh, P. Wahl, S. Burke, and D. Bonn, arXiv:1710.09089 (2017).
 - ²⁷ P. O. Sprau, A. Kostin, A. Kreisel, A. E. Böhmer, P. C. Taufour, V. Canfield, S. Mukherjee, P. J. Hirschfeld, B. M. Andersen, and J. Davis, Science **357**, 75 (2017).

- ²⁸ Z. Du, X. Yang, D. Altenfeld, Q. Gu, H. Yang, I. Eremin, P. J. Hirschfeld, I. I. Mazin, H. Lin, X. Zhu, and H. H. Wen, Nat. Phys **14**, 134 (2017).
- ²⁹ Q. Liu, C. Chen, T. Zhang, R. Peng, Y.-J. Yan, C.-H.-P. Wen, X. Lou, Y.-L. Huang, J.-P. Tian, X.-L. Dong, G.-W. Wang, W.-C. Bao, Q.-H. Wang, Z.-P. Yin, Z.-X. Zhao, and D.-L. Feng, Phys. Rev. X **8**, 041056 (2018).
- ³⁰ S. Borisenko, D. Evtushinsky, Z.-H. Liu, I. Morozov, R. Kappenberger, S. Wurmehl, B. B  chner, A. Yaresko, T. Kim, M. Hoesch, T. Wolf, and N. Zhigadlo, Nature Physics **12**, 311 (2016).
- ³¹ R. Day, G. Levy, M. Michiardi, B. Zwartsenberg, M. Zonno, F. Ji, E. Razzoli, F. Boschini, S. Chi, R. Liang, P. Das, I. Vobornik, J. Fujii, W. Hardy, D. Bonn, I. Elfimov, and A. Damascelli, Phys. Rev. Lett. **121**, 076404 (2018).
- ³² J. Kang and R. M. Fernandes, Phys. Rev. Lett. **117**, 217003 (2016).
- ³³ O. Vafeek and A. V. Chubukov, Phys. Phys. Lett. **118**, 087003 (2017).
- ³⁴ J. S. Hofmann, R. Queiroz, and A. P. Schnyder, Phys. Rev. B **88**, 134505 (2013).

Appendix A: Mean-field order parameters

Using mean-field we decouple eq.(11) into A_{1g} , B_{2g} and E_g pairing channels. The pairing terms for A_{1g} - and B_{2g} -wave states read

$$\begin{aligned}
 \Delta_1^A &= \sum_{\mathbf{q}} \frac{U + J'_{11}}{2} \langle \Psi_{1\downarrow}^T(-\mathbf{q}) \tau_0 \Psi_{1\uparrow}(\mathbf{q}) \rangle + J'_{13} \langle \Psi_{3\downarrow}^T(-\mathbf{q}) \tau_0 \Psi_{3\uparrow}(\mathbf{q}) \rangle \\
 \Delta_3^A &= \sum_{\mathbf{q}} U \langle \Psi_{3\downarrow}^T(-\mathbf{q}) \tau_0 \Psi_{3\uparrow}(\mathbf{q}) \rangle + J'_{13} \langle \Psi_{1\downarrow}^T(-\mathbf{q}) \tau_0 \Psi_{1\uparrow}(\mathbf{q}) \rangle \\
 \Delta_t^A &= -\frac{1}{4} \sum_{\mathbf{q}} \frac{U'_{13} - J_{13}}{2} [\langle \Psi_{3\uparrow}^T(-\mathbf{q}) \Lambda^T \Psi_{1\uparrow}(\mathbf{q}) \rangle + \langle \Psi_{3\downarrow}^T(-\mathbf{q}) \Lambda^\dagger \Psi_{1\downarrow}(\mathbf{q}) \rangle]
 \end{aligned} \tag{A1}$$

$$\begin{aligned}
 \Delta_1^B &= \sum_{\mathbf{q}} \frac{U - J'_{11}}{2} \langle \Psi_{1\downarrow}^T(-\mathbf{q}) \tau_3 \Psi_{1\uparrow}(\mathbf{q}) \rangle \\
 \Delta_3^B &= 0 \\
 \Delta_t^B &= -\frac{1}{4} \sum_{\mathbf{q}} \frac{U'_{13} - J_{13}}{2} [\langle \Psi_{3\uparrow}^T(-\mathbf{q}) \Lambda^\dagger \Psi_{1\uparrow}(\mathbf{q}) \rangle + \langle \Psi_{3\downarrow}^T(-\mathbf{q}) \Lambda^T \Psi_{1\downarrow}(\mathbf{q}) \rangle]
 \end{aligned} \tag{A2}$$

respectively.

Appendix B: E_u -wave state

The odd parity $E_u \otimes U(1)$ p -wave is a novel state which was proposed for intercalated FeSe in Ref. 21. It is a time reversal symmetric topological superconductor which is nodeless for non zero intra-band SOC λ_z . Consequently the order parameter is sensitive to the changes in λ_z and the values for λ_z , p_{z_1} and p_{z_2} need to be adjusted to obey criteria (i)-(iii). These were found in Ref. 21 and are $\lambda_z = -31$ meV, $p_{z_1} = 4179.88$ meV \AA^3 and $p_{z_2} = 2.5p_{z_1}$. This state does not appear in our mean-field analysis. However, for completeness we also calculate the QPI and spin-resolved QPI data for the $E_u \otimes U(1)$ helical p -wave symmetry where the pairing term within the basis of eq.(23) reads

$$\hat{\Delta} = \begin{pmatrix} & -\Delta_{XY}^\dagger & -\Delta_X^\dagger & \\ -\Delta_{XY}^T & & & -\Delta_Y^\dagger \\ \Delta_X^\dagger & & & -\Delta_{XY}^T \\ & -\Delta_Y^\dagger & -\Delta_{XY}^\dagger & \end{pmatrix} \tag{B1}$$

and

$$\Delta_X = \Delta_t \begin{pmatrix} 0 & 1 \\ -1 & 0 \end{pmatrix}, \quad \Delta_Y = \Delta_t \begin{pmatrix} 0 & i \\ -i & 0 \end{pmatrix}, \quad \Delta_{XY} = \Delta_t \begin{pmatrix} \Delta_1 & 0 \\ 0 & i\Delta_3 \end{pmatrix}. \tag{B2}$$

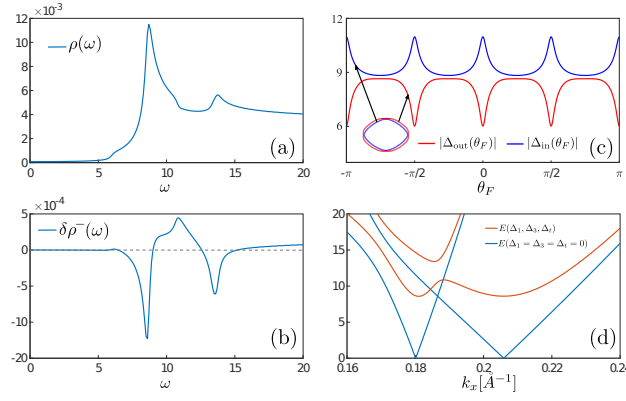


FIG. 8. Figures calculated from Eqs.(24) and (B1) for $E_u \otimes U(1)$ d -wave pairing and (in meV) $\epsilon_1 = -55$, $\epsilon_3 = -105$, $\Delta_1 = 6$, $\Delta_3 = 7$, $\Delta_t = 9$ and $\lambda_{\text{SOC}} = 3$. (a) refers to $\rho(\omega)$, which is fully gaped with two peaks at 8 meV and 14 meV; (b) shows $\delta\rho^-(\omega)$ for a weak (Born) charge impurity. (c) Absolute values of the superconducting gap projected on inner (blue) and outer (red) electron pockets as function of the angle of the Fermi surface, θ_F . (d) Orange curves refer to positive branches of upper and lower superconducting bands along ΓM -direction. Blue curves refer to the same bands for zero superconducting gap. The low-lying energy band has its minima centered above the Fermi-level "back-bending".

In Fig.8(a) and Fig.8(d) we present the DOS and the energy band dispersion for the p -wave state. The DOS show two peaks tuned to lie at 8 meV and 14.3 meV, respectively and the lower energy band shows the back bending. Fig. 8(c) shows the absolute values of Δ_{in} and Δ_{out} projected on the Fermi surface pockets. In Fig.8(b) $\delta\rho^-(\omega)$ is shown. Here, one finds that the main feature of $E_u \otimes U(1)$ in $\delta\rho^-(\omega)$ is that there are two sign changes between the peak energies of the total DOS (i.e. two negative peaks and positive values in between them), which does not agree with experiment²⁸. Therefore this state does not seem consistent with the QPI data at least within Born scattering limit²⁸. For consistency the spin-resolved QPI for the odd parity $E_u \otimes U(1)$ p -state is presented in Fig.9.

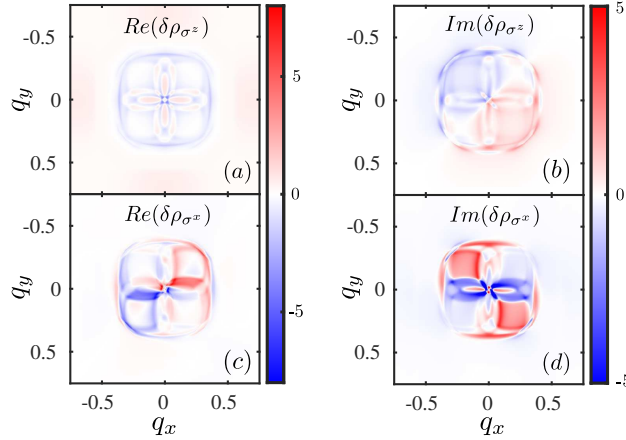


FIG. 9. Spin polarized correction to the LDOS for a magnetic impurity in Born limit. Real and imaginary part of $\delta\rho_{\sigma^z}(\mathbf{q}, \omega)$ (a,d) and $\delta\rho_{\sigma^x}(\mathbf{q}, \omega)$ (c,d) for $E_u \otimes U(1)$ p -wave state at $\omega = 8$ meV.

Appendix C: HAEM'S method for strong inter-band pairing

The SOC induced coupling between the spin singlet and triplet pairing channels translates into a coupling between intra- and inter-band order parameters in band space. It has been argued²¹ that the second peak, seen in STM²⁸ can be at least partially due to an interband gap. In order to investigate how the predictions of HAEM's theory are affected by inter-band pairing we consider a simple model of a two band superconductor with superconductivity

driven by intra- and inter-band pairing.

$$H = \sum_{\mathbf{k}} \Psi^\dagger(\mathbf{k}) \begin{pmatrix} \xi_1(\mathbf{k}) & \Delta_{11} & \Delta_{12} \\ \xi_2(\mathbf{k}) & \Delta_{21} & \Delta_{22} \\ \Delta_{11}^\dagger & \Delta_{21}^\dagger & -\xi_1(\mathbf{k}) \\ \Delta_{12}^\dagger & \Delta_{22}^\dagger & -\xi_2(\mathbf{k}) \end{pmatrix} \Psi(\mathbf{k}) \quad (\text{C1})$$

where $\Psi^\dagger(\mathbf{k}) = (c_1^\dagger(\mathbf{k}) \ c_2^\dagger(\mathbf{k}) \ c_1(-\mathbf{k}) \ c_2(-\mathbf{k}))$. The band dispersions are assumed to be simple parabolic ones $\xi_1(\mathbf{k}) = \frac{k^2}{2m} - \mu_1$ and $\xi_2(\mathbf{k}) = \frac{k^2}{2m} - \mu_2$. Hence, $\xi_2 = \xi_1 - 2B$ with $B = \frac{1}{2}(\mu_2 - \mu_1) > 0$. We only distinguish between intra- and inter-band pairing and neglect for a moment their spin symmetry (i.e. consider them to be spin singlet) to get a better understanding on how the QPI data is affected by the inter-band pairing. We linearize both bands, and calculate $\delta\rho^-(\omega)$ and investigate how it depends on Δ_{12} , the relative phase between Δ_{12} and Δ_{21} and the band offset (direct gap).

1. QPI for Inter-band

We start by examining $\delta\rho^-(\omega)$ for zero intra-band gaps $\Delta_{11} = \Delta_{22} = 0$ and assume $|\Delta_{12}| = |\Delta_{21}|$. From the Green's function $G(\mathbf{k}, \omega)^{-1} = [\omega + i\delta - H_{BdG}]$ we calculate the momentum integrated Green's function as

$$\hat{G}(\omega) = -\pi \frac{\begin{pmatrix} \omega - B & \Delta_{12} \\ 0 & 0 & 0 & 0 \\ 0 & 0 & 0 & 0 \\ \Delta_{12}^\dagger & \omega - B \end{pmatrix}}{\sqrt{|\Delta|^2 - (\omega - B)^2 - i\delta\text{sign}(\omega - B)}} - \pi \frac{\begin{pmatrix} 0 & 0 \\ 0 & \omega + B & \Delta_{21} & 0 \\ 0 & \Delta_{21}^\dagger & \omega + B & 0 \\ 0 & 0 \end{pmatrix}}{\sqrt{|\Delta|^2 - (\omega + B)^2 - i\delta\text{sign}(\omega + B)}} \quad (\text{C2})$$

where $\delta = \delta\text{sign}(\omega)$. The local LDOS we obtain from $\rho(\omega) = -\frac{\text{sign}(\omega)}{\pi} \sum_{i=1}^2 \sum_{\mathbf{k}} \text{Im} \hat{G}(\mathbf{k}, \omega)_{ii}$. The result is

$$\delta\rho^-(\omega) = \text{sign}(\omega) 2N_0^2 \pi \text{Im} \left(\frac{2B^2 - 2\omega^2 + \Delta_{12}\Delta_{21}^\dagger + \Delta_{12}^\dagger\Delta_{21}}{\sqrt{|\Delta|^2 - (\omega - B)^2 - i\delta\text{sign}(\omega - B)} \sqrt{|\Delta|^2 - (\omega + B)^2 - i\delta\text{sign}(\omega + B)}} \right), \quad (\text{C3})$$

which now explicitly includes the interband pair gaps Δ_{12} and Δ_{21} . Eq. (C3) has four poles.

$$\omega_{1,2} = B \pm |\Delta_{12}| \quad (\text{C4})$$

$$\omega_{3,4} = \pm |\Delta_{12}| - B \quad (\text{C5})$$

For $\omega > 0$ one needs to consider the cases: i) $B < |\Delta_{12}|$ and ii) $B > |\Delta_{12}|$ where in the former ω_1 and ω_3 and in the latter ω_2 and ω_4 correspond to the peak energies in $\delta\rho^-(\omega)$.

i) $B < |\Delta|$

In Fig.10, we plot $\delta\rho^-(\omega)$ in arbitrary energy units as a function of ω and $B < |\Delta|$. For $\Delta_{12} = \Delta_{21}$ the behavior of $\delta\rho^-$ is what we define here as “odd”, meaning that between the two intraband gap energies $\delta\rho^-$ changes sign, so the QPI-pattern is s^{++} -like (solid blue curve). In case of $\Delta_{12} = -\Delta_{21}$ $\delta\rho^-$ is “even”, and one obtains as “ s^{+-} -like” pattern (solid orange curve). Hence, if the inter-band gap is larger than the band offset HAEM is sensitive to the relative phase between Δ_{12} and Δ_{21} .

ii) $B > |\Delta|$

If $B > |\Delta_{12}|$ the situation is a different one as can be seen by the dotted curves in Fig.10. In both cases $\Delta_{12} = \pm\Delta_{21}$ and $\delta\rho^-$ is “odd”, mimicking an s^{++} -pattern. Consequently, HAEM's method is *not* sensitive to the relative phase between Δ_{12} and Δ_{21} . Therefore, in a system with a large dominant inter-band gap the QPI signal depends not only on the relative phase between Δ_{12} and Δ_{21} but also on the ratio between $|\Delta|$ and B , hence on the band structure.

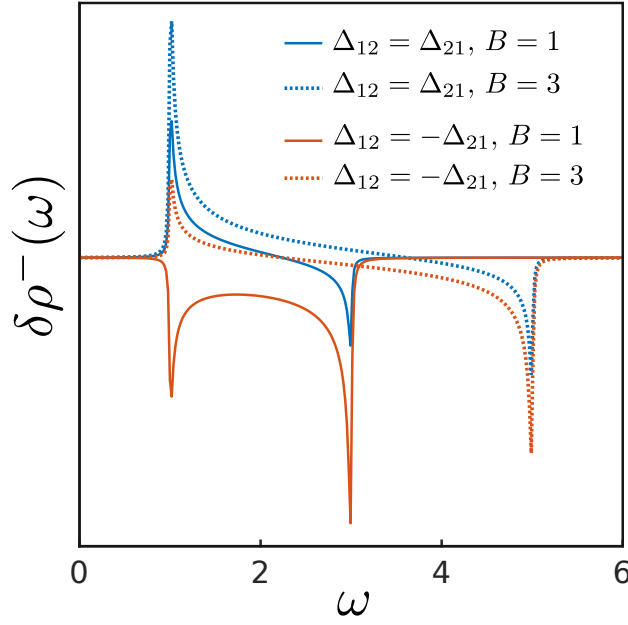


FIG. 10. $\delta\rho^-(\omega)$ in arbitrary energy units for the two cases (i) $B < |\Delta_{12}| = 2$ (solid curves) and (ii) $B > |\Delta_{12}| = 2$ (dotted curves). (i): QPI pattern is sensitive to phase difference showing s^\pm -pattern for $\Delta_{12} = -\Delta_{21}$ and s^{++} -pattern for $\Delta_{12} = \Delta_{21}$. (ii): Both $\Delta_{12} = \pm\Delta_{21}$ exhibit s^{++} -pattern.

2. Inter+Intra-Band

The influence of the inter-band gap on the QPI does affect the HAEM results on sign-changing and sign preserving intra-band gaps. To show this we numerically present the $\delta\rho^-(\omega)$ for $\Delta_{11} \neq \Delta_{22}$ and $\text{sign}(\Delta_{11}) = -\text{sign}(\Delta_{22})$ leading to an initial s^\pm pattern. Then we increase $|\Delta_{12}|$ and show that at a certain magnitude the phase information is lost. The results are plotted in Fig.11 where in the left and right panel we have $\Delta_{12} = -\Delta_{21}$ and $\Delta_{12} = \Delta_{21}$, respectively. Our results for the LDOS are presented in Fig.11(a) and Fig. 11(b). If $\Delta_{12} = 0$, see orange curve, only intra-band

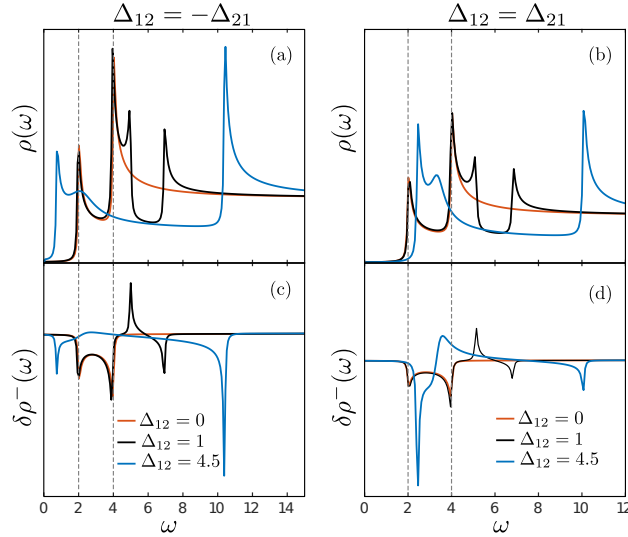


FIG. 11. $\rho(\omega)$ and $\delta\rho^-(\omega)$ as function of ω for various values of Δ_{12} . Data shown for $\Delta_{12} = -\Delta_{21}$ [(a) and (c)] and $\Delta_{12} = \Delta_{21}$ [(b) and (d)], respectively. Intra-band gaps and band offset are $\Delta_{11} = 2$, $\Delta_{22} = -4$ and $B = 5$. Vertical dashed lines mark energies of intra-band gaps

gaps $\Delta_{11} = 2$ and $\Delta_{22} = -4$ are present which cause a two peak feature in the LDOS which we call peak 1 and 2. If we switch the inter-band pairing $\Delta_{12} = 1$ on, see black curves, peak 3 and 4 appear as a consequence of inter-band

pairing, whereas peak energies 1 and 2 are only slightly affected. If Δ_{12} is increased further, see blue curves, peak 2 and 3 merge.

In the absence of inter-band pairing the QPI pattern in Fig.11(c)-(d) is of s^\pm type, see orange curve. For moderate values $\Delta_{12} = 1$ one can nicely distinguish between intra- and inter-band contributions. Peak 1 and 2 show an s^\pm pattern due to the sign change between Δ_1 and Δ_2 , whereas between peak 3 and 4 the pattern is an s^{++} since the inter-band gap is smaller than the band offset B , see Fig.10. For moderate values of Δ_{12} , see blue curves, peak energies 1 and 2 start to deviate from Δ_1 and Δ_1 as marked by the vertical dashed lines. As soon as peak 2 and 3 merge the s^\pm pattern between peak 1 and peak 2 becomes more and more difficult to resolve. The blue curve corresponds to the situation where the inter-band gap Δ_{12} is larger than the intra-band gap but smaller than the band offset. The latter condition causes an s^{++} pattern between peak 3 and 4 independent of the relative phase between Δ_{12} and Δ_{21} , see C.1. This is accompanied by Δ_{11} and Δ_{22} having a s^\pm symmetry. The combination of both patterns leads to a sign-change of $\delta\rho^-(\omega)$ in the region $2 < \omega < 4$ which might be misinterpreted as an s^{++} pattern between Δ_{11} and Δ_{22} and hence carries no concrete phase information.